Hybrid MPI-MRI System for Dual-Modal *In Situ* Cardiovascular Assessments of Real-Time 3D Blood Flow Quantification—A Pre-Clinical *In Vivo* Feasibility Investigation

Jochen Franke, Nicoleta Baxan, Heinrich Lehr, Ulrich Heinen, Sebastian Reinartz, Jörg Schnorr, Michael Heidenreich, Fabian Kiessling, and Volkmar Schulz

***Abstract*— Non-invasive quantification of functional parameters of the cardiovascular system, in particular the heart, remains very challenging with current imaging techniques. This aspect is mainly due to the fact, that the spatio-temporal resolution of current imaging methods, such as Magnetic Resonance Imaging (MRI) or Positron Emission Tomography (PET), does not offer the desired data repetition rates in the context of real-time data acquisition and thus, can cause artifacts and misinterpretations in accelerated data acquisition approaches. We present a fast non-invasive and quantitative dual-modal *in situ* cardiovascular assessment using a hybrid imaging system which combines the new imaging modality Magnetic Particle Imaging (MPI) and MRI. This pre-clinical hybrid imaging system provides either a 0.5 T homogeneous B_0 field for MRI or a 2.2 T/m gradient field featuring a Field-Free-Point for MPI. A comprehensive coil system allows in both imaging modes for spatial encoding, signal excitation and reception. In this work, 3-dimensional anatomical information acquired with MRI is combined with *in situ* sequentially acquired time-resolved 3D (i.e. 3D + t) MPI bolus tracking of superparamagnetic iron oxide nanoparticles. MPI data were acquired during a 21 μl (40 μmol(Fe)/kg$_{BW}$) bolus tail vein injection under free-breathing with an ungated and non-triggered MPI scan with a repetition rate of 46 volumes per seconds. We successfully determined quantitative hemodynamics as 3D + t velocity vector estimations of a beating rat's heart by analyzing 3 seconds of 3D + t MPI image data. The used hybrid system allows for MR-based MPI Field-of-View planning and cardiac cross-sectional anatomy analysis, precise co-registration of dual-modal datasets, as well as for MPI-based hemodynamic functional analysis using an optical flow technique. We present the first *in-vivo* results of a new methodology, allowing for fast, non-invasive, quantitative and *in situ* hybrid cardiovascular assessment, showing its potential for future clinical applications.**

***Index Terms*— Cardiovascular assessment, data fusion, flow quantification, hemodynamics, hybrid imaging system, magnetic particle imaging (MPI), magnetic resonance imaging (MRI), multi-modality, real-time, 3D + t flow analysis.**

Manuscript received March 26, 2020; revised July 23, 2020; accepted August 6, 2020. Date of publication August 17, 2020; date of current version November 30, 2020. This work was supported in part by the German Federal Ministry of Education and Research under Grant FKZ 13N11088 and in part by the Animal Ethics Committee (Regional Council of Karlsruhe), Germany, under Grant 35-9185.81/G-178/12. *(Corresponding authors: Jochen Franke; Volkmar Schulz.)*

Jochen Franke is with the Preclinical Imaging Division, Bruker BioSpin MRI GmbH, 76275 Ettlingen, Germany, and also with the Department Physics of Molecular Imaging Systems, RWTH Aachen University, 52074 Aachen, Germany (e-mail: jochen.franke@bruker.com).

Nicoleta Baxan was with the Preclinical Imaging Division, Bruker BioSpin MRI GmbH, 76275 Ettlingen, Germany. She is now with the Biological Imaging Centre, Imperial College London, London SW7 2AZ, U.K. (e-mail: n.baxan@imperial.ac.uk).

Heinrich Lehr and Michael Heidenreich are with the Preclinical Imaging Division, Bruker BioSpin MRI GmbH, 76275 Ettlingen, Germany (e-mail: heinrich.lehr@bruker.com; michael.heidenreich@bruker.com).

Ulrich Heinen was with the Preclinical Imaging Division, Bruker BioSpin MRI GmbH, 76275 Ettlingen, Germany. He is now with the Department of Medical Engineering, Pforzheim University of Applied Sciences, 75175 Pforzheim, Germany (e-mail: ulrich.heinen@hs-pforzheim.de).

Sebastian Reinartz is with the Department of Diagnostic and Interventional Radiology, University Hospital Aachen, 52074 Aachen, Germany (e-mail: sebastian.reinartz@pmi.rwth-aachen.de).

Jörg Schnorr is with the Department of Radiology, Charité University Hospital Berlin, 10117 Berlin, Germany (e-mail: joerg.schnorr@charite.de).

Fabian Kiessling is with the Department of Experimental Molecular Imaging, RWTH Aachen University, 52074 Aachen, Germany (e-mail: fkiessling@ukaachen.de).

Volkmar Schulz is with the Department Physics of Molecular Imaging Systems, RWTH Aachen University, 52074 Aachen, Germany (e-mail: volkmar.schulz@pmi.rwth-aachen.de).

This article has supplementary downloadable material available at https://ieeexplore.ieee.org, provided by the authors.

Color versions of one or more of the figures in this article are available online at https://ieeexplore.ieee.org.

Digital Object Identifier 10.1109/TMI.2020.3017160

I. Introduction

MULTIMODAL imaging systems are very powerful diagnostic tools for a better understanding of the origin of diseases and the development of new forms of therapy, as they combine highly complementary information [1]. The gain in information above all consists in measuring functional, molecular and morphological parameters and thus increasing the spatial and temporal correspondence of multiparametric diagnostic information. One of the first hybrid approaches, which is already routine in clinical practice, is the combination of PET and computed tomography (CT) [2]. Hybrid PET-MRI systems have been used for pre-clinical research and have recently emerging as clinical routine hybrid systems for human applications [3], [4]. For example, PET-CT and PET-MRI combine detailed anatomical information determined with CT or MRI with tracer dependent functional parameters quantified by PET, such as the metabolism of glucose. Diagnostic

findings in fast biological processes, such as pathological myocardial movement, valvular heart diseases or stenosis require fast acquisition schemes found in e.g. ultrasound. Recently, accelerated MR-based imaging sequences have been presented in [5], allowing for free-breathing cine MRI data acquisition. Whilst the reconstructed temporal resolution is superb, the overall scan time is in the range of minutes as these methods still necessitate physiological gating and triggering to cope with the slow encoding scheme.

In 2005, Gleich and Weizenecker presented a novel tracer-based imaging modality called Magnetic Particle Imaging (MPI) [6], which allows the measurement of the distribution of e.g. superparamagnetic iron oxide nanoparticles (SPION) in three dimensions (3D) with high temporal resolution. In brief, MPI uses a static magnetic gradient field called *Selection Field* featuring a Field-Free-Region and a superimposed time variant homogeneous magnetic field, called *Drive Field*. Due to the *Selection Field* properties in combination with the non-linear magnetization behavior of the SPIONs, the time-varying SPION signal induced in the receiver coils allow to reconstruct the SPIONs spatial distribution. This is due to the effect that SPIONs stay saturated far away from the Field-Free-Region, while the magnetization of the SPIONs close to the Field-Free-Region change rapidly and non-linearly by the *Drive Field* excitation. From this acquired time-varying voltage signal, the tracer distribution in the Field-of-View (FoV) can be reconstructed quantitatively using different techniques, in particular by solving the imaging equation using the system matrix approach [6], [7]. As a result, the reconstructed images contain functional information of the time-resolved 3D (i.e. 3D + t) quantitative tracer distribution within the FoV. MPI is highly sensitive to the non-linear SPION response and the acquired data possess a high signal-to-noise-ratio (SNR) with no background signal generated by e.g. biological tissue. First approaches to use MPI as a functional and molecular imaging modality have been presented in [8], [9]. Multi-frequency excitations as shown in [10] further increase the access to molecular and physiological processes.

A multi-modal dataset combining MPI and MRI data was shown in [11] for the first time. This multi-modal dataset comprised the temporal quantitative tracer distribution in a beating mouse heart fused with a static morphological MRI reference dataset offering a good soft tissue contrast. Recently, other multi-modal MPI applications have been presented [9], [12]–[15]. All these aforementioned multi-modal *in vivo* studies were, however, conducted using two independent stand-alone imaging systems involving significant workflow overheads and complex animal handling with the need for fiducial markers to facilitate multi-modal image co-registration with the required spatio-temporal fidelity.

To reduce co-registration errors induced by object transportation and/or repositioning between different modalities, as well as to circumvent the obstacles using fiducial markers, several hybrid MPI scanner designs were introduced [16]–[22]. Hybrid imaging systems facilitate at least sequential multi-modal data acquisition with a straight-forward and well-defined object positioning at most. While these hybrid designs have so far only been proven and characterized by phantom experiments, the scope of this work is to translate the multi-modal capability of the system described in [20] into the first *in situ* dual-modal cardiovascular assessment on rodents. This was realized in this study by exploiting the MRI-mode of a highly integrated MPI-MRI hybrid system [20] for precise subject positioning, dual-modal FoV-planning and acquisition of high-spatial morphological information, while the MPI-mode facilitated *in situ* sequential acquisition of time-resolved 3D MPI bolus tracking of superparamagnetic iron oxide nanoparticles. Based on these input data, 3D + t fast MPI-based quantitative hemodynamic velocity reconstruction of a beating rat's heart under free breathing is reported for the first time making use of MRI-derived anatomical information for a detailed structural analysis.

II. Methods

The dual-modal *in vivo* cardiovascular assessment on a rat was conducted using a highly integrated MPI-MRI hybrid system (Bruker BioSpin MRI GmbH, Germany) described and characterized in [20]. In brief, this hybrid MPI-MRI system shown in Fig. 1 allows pre-clinical MPI and MRI imaging of small rodents in a sequential manner by usage of a dual-mode main magnetic field generator. A comprehensive coil system allows for spatial encoding, signal excitation and signal reception in both imaging modes. The symmetrically and concentrically arranged system design offers an open bore diameter of 130 mm before insertion of the MRI trans-receive (TRx) radio-frequency (RF) coil with an inner diameter of 60 mm. The dual-mode main magnetic field generator allows for either a homogeneous B_0 field with a maximal field strength of approx. 0.5 T fulfilling the magnetic field requirements for MRI or a steep magnetic gradient field with a maximal gradient strength of 2.2 T/m forming a Field-Free-Point (FFP) dedicated to MPI. Typical modality transition time is in the range of 2 min in either direction. Seamless multi-modal MPI-MRI studies without the need for any object repositioning is facilitated by the spatial match of the two respective FoV centers, as well as by using one adapted ParaVision 6.1 software (Bruker BioSpin MRI GmbH, Germany) suitable for both imaging modalities. In combination, this provides significant benefits for *in vivo* studies in which precise targeted imaging is mandatory. Thus, this hybrid system allows for MPI FoV planning on the basis of morphological information acquired with MRI along with high-spatial and temporal confidence in dual-modal dataset fusion.

As shown in the schematic flow chart in Fig. 2, the experiment reported in this contribution was conducted in four main parts, namely: (1) pre-injection morphological MRI examination, (2) MPI examination with bolus injection, (3) post-injection morphological MRI examination and (4) data post-processing. These four main parts will be described in-depth in the subsequent sections.

A. Experimental Part: MRI-Based Morphology Assessment and Targeted Subject Positioning

1) Animal Preparation and Handling: One rat (Lewis, 260 g body weight) was anesthetized (Isoflurane rate approx.

Fig. 1. Photograph of the highly integrated MPI-MRI hybrid system (Bruker BioSpin MRI GmbH, Germany) described and characterized in [20]. The dual-mode main magnetic field generator used in this study features a MRI-modus with $B_0 = 0.495$ T or $G_Z = 2.2$ T/m in the MPI-modus. In addition, a three-axis MRI gradient, a 2^{nd} order shim coil set, a TRx radio-frequency MRI coil and a TRx three-axis *Drive Field* coil are embedded allowing for seamless dual-modal examinations.

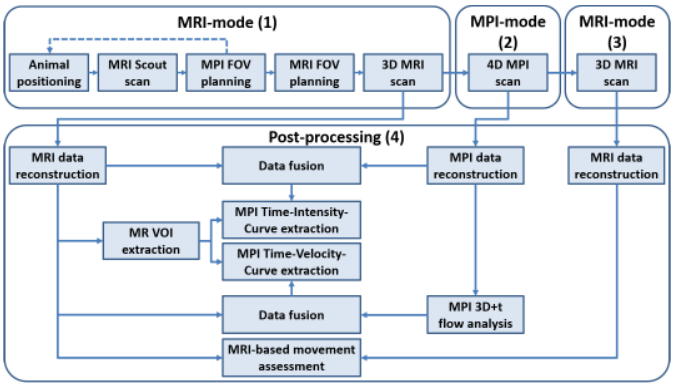

Fig. 2. Schematic flow chart of the experimental dual-modal *in vivo* cardiovascular assessment, which was performed in 4 main parts in the order: (1) MRI-based MPI-FoV planning and high-spatial resolution MRI morphological assessment (2) 3D + t MPI data acquisition including manual SPION administration (3) post-injection high-spatial resolution MRI morphological data acquisition and (4) post-processing steps including data reconstruction, hybrid data fusion and MPI-based 3D + t velocity vector estimation.

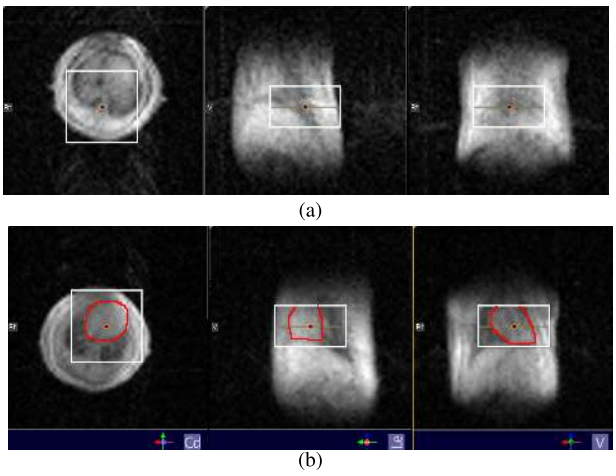

Fig. 3. Low-spatial resolution tri-planar FLASH MRI images (LEFT: axial, CENTER: sagittal, RIGHT: coronal view) used for MR-based animal positioning. The animal cradle was repositioned manually to place the target morphology i.e. the heart chambers (highlighted in red for visual guidance) into the non-relocatable MPI-FoV. (a)-(b) different animal positions are shown in the ParaVision GUI with the non-relocatable MPI-FoV depicted as overlays. The final subject position (b) was preserved during the entire dual-modal cardiovascular assessment.

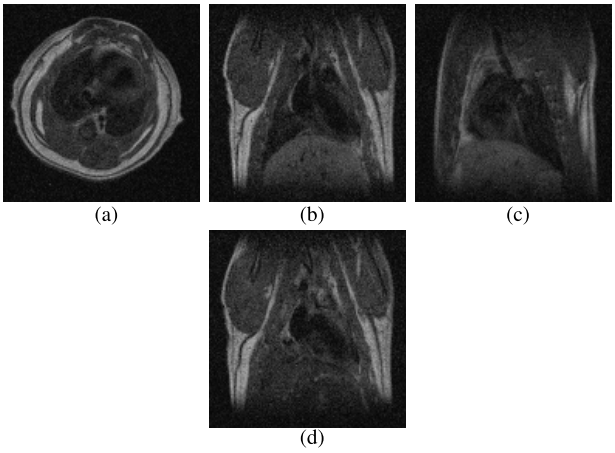

Fig. 4. One representative slice of the high-spatial resolution morphological reference MRI datasets, acquired with an MSME sequence in an (a) axial, (b) coronal and (c) sagittal slice orientation prior to the MPI tracer injection. (d) depicts the coronal post-injection dataset (acquired approx. 40 *min* after injection of 21 μl undiluted Resovist) of the same slice as shown in (b). Note the hypo-intense signal areas caused by SPION accumulation, especially in the liver.

1.7 vol%, air flow rate approx. 0.6 l/min) and centered within the MPI-MRI hybrid scanner after a system warm-up phase to thermal equilibrium. The animal was kept under continuous supervision of vital parameters, i.e. temperature and respiration at a respiration rate of approx. 40−60 bpm and heart rate in the range of 280−360 bpm by manual adjustment of the Isoflurane flow rate.

2) MR-Based Animal Positioning: In the MRI mode of the hybrid system with a polarization field strength of $B_0 = 0.495$ T, low-spatial resolution tri-planar MRI datasets were acquired (FLASH, TE/TR = 2.8/100 ms, matrix = 64 × 64, FoV = 80×80 mm^2, slice thickness = 10 mm, slice orientations: axial/coronal/sagittal, NEX = 2, FA = 30°, scan time = 12 s). These orthogonal low-spatial resolution datasets were used to position the target region within the non-relocatable MPI-FoV. This MR-based geometry planning procedure accounted for the predetermined global translation [23] (−2.5 mm, −1 mm, −1.5 mm for X-, Y- and Z-direction, respectively), compensating a residual but constant system specific coordinate system offset of the two respective modalities. Using the MRI morphology information, the animal cradle position was shifted manually centering the heart as the target imaging region within the pre-defined static 3D MPI-FoV. The final subject position was preserved during the entire dual-modal cardiovascular assessment.

3) High-Spatial Resolution Morphological Reference Datasets: A 1^{st} and 2^{nd} order global shim was optimized using an automatic Free-Induction-Decay (FID) based algorithm including an automatic re-adjustment of the basic frequency. Three orthogonal MRI 2D Multi-Slice Multi-Echo (MSME) spin echo datasets (TE/TR = 8.6/300 ms, matrix = 128 × 128 × 9, FoV = 50 × 50 × 27 mm^3, BW = 25 kHz, slice orientations: axial/coronal/sagittal,

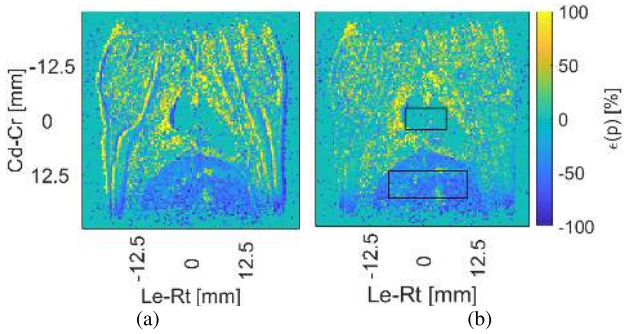

Fig. 5. MRI-based movement assessment comparing the pre- and post-injection high-resolution MRI MSME dataset shown in Fig. 4b and 4d. This error map is a measure for signal stability, animal position sustainability, as well as SPION accumulations. (a) using the original data, (b) using the post-injection data shifted by one pixel in Le-Rt (readout) direction. In (b), two regions-of-interest within the heart (blood-pool dominated) and the liver tissue used for data analysis are presented.

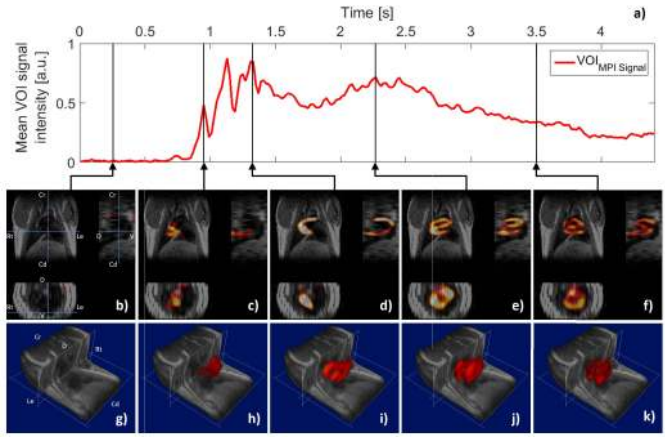

Fig. 6. Hybrid dataset comprising the coronal 3D high-spatial resolution MSME MRI dataset (grayscale) and the 3D + t MPI dataset (redscale). (a) depicts the main bolus passage as spatio-mean MPI signal intensity over time (i.e. the Time-Intensity-Curve) of the reconstructed MPI repetitions (repetition 130 − 350, TR = 0.021 s). (b)-(f) show orthogonal views of the hybrid dataset for selected time points. (g)-(k) depict a volume rendered representation of the respective time-points. Videos of the orthogonal and volume rendered visualization are provided as supplementary material ***S1*** and ***S2*** to this manuscript.

NEX = 25, scan time = 16 min) were acquired sequentially serving as high-spatial resolution morphological reference datasets.

B. Experimental Part: MPI Examination With Bolus Injection

The hybrid MPI-MRI system was converted into the MPI mode by switching the dual-mode main magnetic field generator coil polarity configuration. Neither any animal handling, animal repositioning, nor system hardware modifications were necessary. Thereafter, a time-resolved 3D MPI experiment ($A_{\mathrm{DF\,x,y,z}} = 12\,\mathrm{mT}$, $G_{\mathrm{SF\,max}} = 2.2\,\mathrm{T/m}$, BW = 625 kHz, TR = 21.54 ms, repetitions = 3000, AVG = 1) was started prior to a manual tail vein administration of a bolus of 21 μl undiluted Resovist (Bayer Schering Pharma AG, Germany) which corresponds to a dosage of 40 $\mu\mathrm{mol(Fe)/kg_{BW}}$.

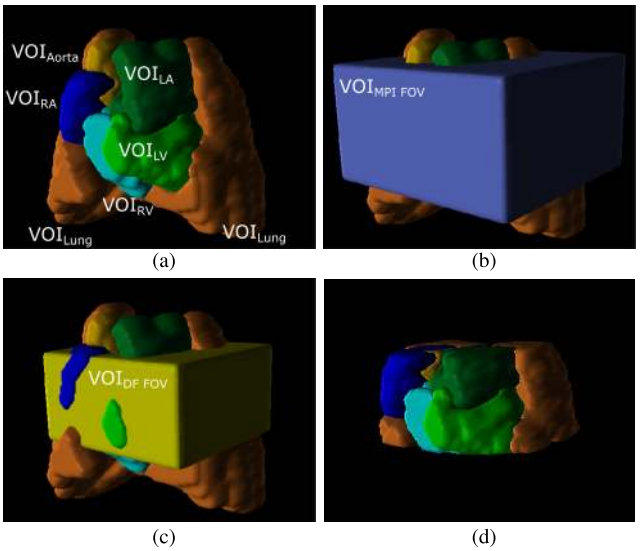

Fig. 7. MR-derived VOIs of the right atrium (RA), right ventricle (RV), left atrium (LA), left ventricle (LV), as well as the lungs. The manual segmentation was performed on the high-spatial resolution coronal MRI dataset. Each VOI is presented in a color-coded volume rendered representation. (a) depicts the complete anatomical VOIs (b) furthermore presents the reconstructed MPI-FoV, while (c) presents the DF-FoV defining the confidence interval of the reconstructed MPI data, while (d) shows the MR-derived VOIs cropped along the DF-FoV. The cropped VOIs were used in this study for MPI data analysis.

TABLE I

VOLUMES OF THE RECONSTRUCTED $\mathrm{MPI_{FOV}}$, THE $\mathrm{DF_{FOV}}$ AS WELL AS THE MPI SIGNAL INTENSE VOLUME DERIVED BY MANUAL THRESHOLDING. FURTHERMORE, MR-DERIVED ANATOMICAL VOIS DEPICTING THE ENTIRE RIGHT AND LEFT ATRIUM (RA, LA), RIGHT AND LEFT VENTRICLE (RV, LV), AS WELL AS THE LUNGS ARE GIVEN. IN ADDITION, THE VOLUMES OF THE ANATOMICAL VOIS CROPPED ALONG THE MPI $\mathrm{DF_{FOV}}$ ARE PRESENTED NEXT TO THE RATIO BETWEEN BOTH VERSIONS. THE VOLUME NOT ASSIGNED TO ANY OF THE AFOREMENTIONED ANATOMICAL VOIS WITHIN THE $\mathrm{DF_{FOV}}$ IS LISTED, TOO

VOI name	VOI volume [ccm]	$\mathrm{VOI_{cropped}}$ volume [ccm]	ratio [1]
$\mathrm{MPI_{FoV}}$	12.54	5.18	0.41
$\mathrm{DF_{FoV}}$	5.18	5.18	1.00
MPI Signal	n.a.	0.73	1.00
Right atrium (RA)	0.64	0.57	0.89
Right ventricle (RV)	0.28	0.22	0.79
Left atrium (LA)	0.64	0.47	0.73
Left ventricle (LV)	0.48	0.44	0.92
Lungs	6.43	1.94	0.30
not assigned	n.a.	1.54	1.00

C. Experimental Part: Post-Injection MRI

Again without any animal handling, animal repositioning or system hardware modifications, the system was converted into the MRI mode featuring a polarization field strength of $B_0 = 0.495\,\mathrm{T}$. A latency to the tracer injection of approx. 40 min was conducted to allow the accumulation of the administered tracer material in the liver tissue. To reduce susceptibility artifacts caused by the iron-loaded liver, the 1^{st} and 2^{nd} order global shim was optimized as previously

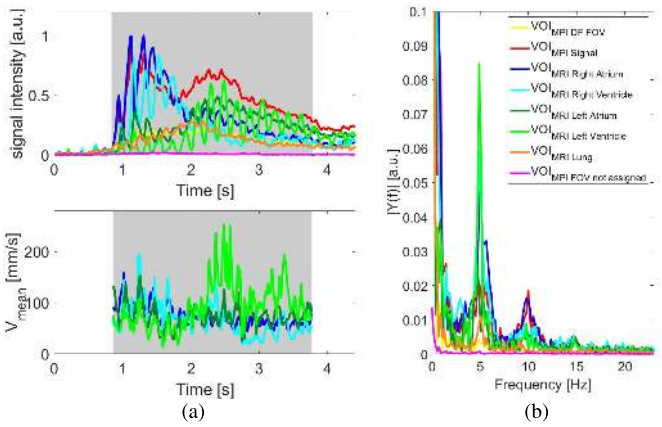

Fig. 8. Dynamic first-pass of the administered SPION bolus, represented as TICs and the corresponding power spectra showing the SPION concentration. Additionally, the TVCs show the velocity evolution estimated from the reconstructed MPI image data. The 3D MPI-FoV was recorded with a temporal resolution of 21.54 ms/volume and reconstructed in a post-processing step with an isotropic spatial resolution of $1 \times 1 \times 1$ mm^3. From this data, an optical flow analysis was performed to estimate a velocity vector field. (a) TOP: TVCs for different VOIs derived from high-spatial resolution MR anatomical reference data or derived from the MPI data itself. BOTTOM: TVCs extracted from the velocity vector field for different VOIs derived from high-spatial resolution MR anatomical reference data. (b) Power spectrum computed from the TICs of the four heart chambers RA, RV, LA and LV, as well as the lungs. The color-coding is identical for all three plots.

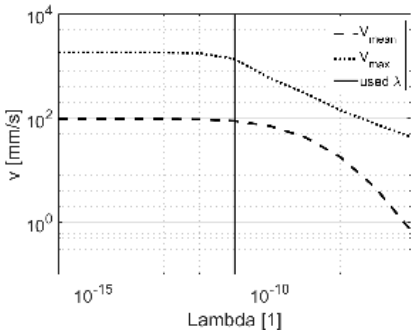

Fig. 9. Reconstructed spatio-temporal mean and maximum velocity of 12 consecutive repetitions as function of the used Tikhonov optical flow regularizer λ. Based on this graph, $\lambda = 10^{-11}$ was chosen manually to preserve stable flow estimation and to circumvent flow velocity underestimation.

described. One coronal MSME experiment, described above, was repeated serving as post-injection high-spatial resolution morphological reference dataset to validate the SPIONs accumulation in the liver, as well as animal position consistency with respect to the pre-injection coronal MSME dataset.

D. Data Post-Processing and Data Analysis

1) MPI Dataset Reconstruction: The dynamics highlighting the first bolus passage through the heart were selected manually from the MPI raw data stream by examination of the time evolution of one frequency component. Prior to a system matrix based MPI image reconstruction [24], the average background signal was derived from the MPI raw data stream prior to the bolus passage and subtracted from all repetitions. For image reconstruction, a Kaczmarz [25] algorithm with physical constraints enforcing positive and real values was set up in the software ParaVision 6.1 (iterations = 60, relative regularization $\lambda = 8 \cdot 10^{-3}$, max. frequency mixing order = 25, SNR threshold = 10, resulting in 2932 used frequencies, averaging = no) using a denoised isotropic system matrix [26] featuring a spatial overscan [27] (matrix = $28 \times 28 \times 16$, FoV = $28 \times 28 \times 16$ mm^3, DF-FoV = $22 \times 22 \times 11$ mm^3) of the corresponding tracer material. The reconstructed MPI data was exported into DICOM-format for post-processing steps described hereafter.

2) Dataset Fusion: For image fusion, the image analysis software PMOD 3.7 (PMOD Technologies LLC, Switzerland) was used. The high-spatial resolution MSME 3D MRI data was loaded in the DICOM-format, interpolated to an isotropic resolution of $0.39 \times 0.39 \times 0.39$ mm^3 and zero-padded to ensure coverage of the entire MPI FoV. Next the 3D + t MPI dataset was loaded, fused and re-gridded to the coronal MSME MRI dataset. A pre-determined global translation [23] (-2.5 mm, -1 mm, -1.5 mm for X-, Y- and Z-direction, respectively) was applied to the MPI data to co-registrate both datasets by compensating a residual but constant system specific coordinate system offset of the two respective modalities. This fused and co-registered hybrid dataset was used for all further hybrid post-processing steps.

3) MRI-Based Movement Assessment: To confirm a stable subject position during the entire *in situ* dual-modal cardiac examination, the original non-interpolated pre- and post-injection coronal high-resolution MSME MRI datasets were compared. The percental error-map $\epsilon(p)$ was computed using MATLAB (The MathWorks, Inc., USA) by:

$$\epsilon(p) = \frac{I_{\text{post}}(p) - I_{\text{pre}}(p)}{I_{\text{pre}}(p)} \cdot 100 \qquad (1)$$

where $I_{\text{pre}}(p)$ and $I_{\text{post}}(p)$ are the image intensities of the respective MSME dataset at the spatial position p.

4) Hybrid Dataset Visualization: Using PMOD, the co-registered datasets were visualized in orthogonal views, as well as volume-rendered by applying a manually determined threshold. Two different color-maps were used for the MRI (grayscale) and the MPI (redscale) data and a time-resolved sequence was generated including cut-planes in the volume-rendered MRI dataset.

5) MR Segmentation and Anatomical Volume-of-Interest Extraction: From the pre-injection high-spatial resolution morphological coronal reference MRI dataset, static Volumes-of-Interest (VOIs) were segmented manually using PMOD. VOIs were generated for: the right and left atrium (RA, LA), right and left ventricle (RV, LV), the lungs as well as all other voxels not assigned to any of the afore mentioned VOIs but which are contained within the Drive-Field FoV (DF-FoV). All VOIs were cropped along the DF-FoV, i.e. the volume spanned up by the FFP-trajectory during MPI data acquisition (in this case $22 \times 22 \times 11$ mm^3, for X-, Y- and Z-direction, respectively) which defines the confidence interval where the MPI reconstruction produces faithful images [27].

6) MPI Time-Intensity-Curve Analysis: Besides the anatomical MRI-derived VOIs, MPI-derived VOIs representing the entire MPI-FoV, the DF-FoV, as well as a static thresholded

MPI signal derived VOI were generated. The MPI signal VOI was extracted by averaging the entire dynamic MPI information to a single repetition and utilization of a manually selected threshold. For each MRI- and MPI-derived VOI, one Time-Intensity-Curve (TIC) was extracted from the co-registered 3D + t MPI dataset, representing the spatio-mean signal intensity and thus tracer concentration over time. Fourier analysis was used to examine the individual TICs in frequency space.

7) 3D + t MPI Flow Analysis and Visualization: For cardiac 3D + t hemodynamic investigation of the 3D + t MPI image data, a Flow Analysis Toolbox [28]–[30] was used. In brief, this flow analysis, implemented in MATLAB, exploits the pseudo-periodic information of modulated tracer wave fronts in image space to extract the tracer wave front propagation by means of an Optical Flow analysis [31]. Using the wave front propagation information and the sampling frequency, a 3D + t real-time velocity vector field can be deduced.

As blood flow occurs in answer to the periodic myocardial wall contraction, revealing a pseudo-periodic tracer concentration, this tool uses time and frequency signal processing approaches to extract and filter TICs from a reconstructed MPI dataset for each point in space (p) and point in time (t). By frequency filtering of the extracted TIC spectra, only signals within a narrow band around the tracer pulse frequency (i.e. the cardiac frequency) and its harmonics up to an user defined threshold was used for the flow reconstruction by means of the optical flow equation [31]:

$$\nabla I(p,t) \cdot v + \frac{\partial I(p,t)}{\partial t} = 0 \tag{2}$$

Here, $I(p,t)$ is the image intensity for each voxel over time, i.e. the time-depended tracer-distribution, within the 3D + t MPI dataset. To circumvent the pitfall of spatio-temporal extrema of the TICs - where time- and space-derivative nullifies - the Hilbert transform is used to complement the processed TICs by creating a quadrature signal. The quadrature signal is in fact a time-shifted signal of the original sequence that undergoes a phase shift of $\pi/2$. With this, a representation of the signal at every point in space p within the FoV is preserved by a time dependent instantaneous phase $\phi(p,t)$, as well as an instantaneous modulation depth $M(p,t)$, called henceforward modulus. To adapt the optical flow equation from the intensity representation to the phase representation [28], one can re-write Eq. 2 to:

$$\nabla \phi(p,t) \cdot v + \frac{\partial \phi(p,t)}{\partial t} = 0 \tag{3}$$

where $\phi(p,t)$ is the phase of the modulated tracer wave front for each point in space (p) and point in time (t). Using Eq. 3, 3D + t velocity vector estimations can be derived by estimating the unknown wave front displacement by means of the Lukas-Kanade method [31] which assumes Eq. 3 to hold true in a pre-defined neighborhood. By inversion of a system of equations of size 3×3, this problem can be solved allowing the estimation of quantitative velocity vector fields.

For cardiac assessment shown in this contribution, the cardiac frequency was first derived automatically from the reconstructed 3D + t MPI image data (frame $40 - 180$, marked gray in Fig. 8) by Fourier analysis. Using this modulation frequency, the TIC for each voxel was narrow-band filtered with a bandwidth containing the information up to the third harmonic of the modulation frequency. This sequence was fed into the above described MPI Flow Analysis Toolbox to first adjust for the Tikhonov optical flow regularizer λ by reconstruction of a short sub-sequence containing 12 consecutive 3D volumes and thus, approximately one cardiac cycle. Flow estimation was performed in this sub-sequence using a variable Tikhonov optical flow regularizer in the range of $\lambda = 10^{-16} - 10^{-6}$. As suggested in [30], the mean and the max absolute velocity value within the reconstructed volume were analyzed as a function of λ. This regularization-depended behavior was used to define the lowest λ, which on the one hand results in a minimal underestimation of the reconstructed velocity field, as well as circumvents local overestimates. This pre-defined λ was used thereafter to compute a flow estimation with a time resolution of 10 ms for the entire image sequence (frame $40 - 180$, marked gray in Fig. 8). The resulting MPI-derived real-time 3D + t velocity vector field was analyzed as Time-Velocity-Curves (TVCs). By using the MR-derived VOIs the spatio-mean velocity $\vec{v}(t)$ was automatically extracted and plotted in the form of the absolute magnitude for each heart chamber (RA, RV, LA and LV, respectively). For morphological guidance, the MPI-derived real-time 3D + t velocity vector field, represented as velocity color-coded streamlines, was superimposed with the three orthogonal high-resolution MRI datasets. For this, the three MRI datasets, as well as the 3D + t velocity vector field were interpolated to an isotropic resolution of $0.39 \times 0.39 \times 0.39$ mm^3 prior to visualization.

To sort the real-time 3D + t velocity vector field into one representative cardiac cycle, the time-points of individual cardiac cycles were determined manually from the real-time TIC of the RA, compensating the lack of electrocardiogram data. Using this time information, the reconstructed real-time velocity vector field was retrospectively gated by sorting the real-time sequence into one representative virtual cardiac cycle. This representative cardiac cycle with 21 bins with a 10 ms time resolution was analyzed by means of the local evolution in the MR-derived VOIs. For this, TVCs were plotted in the form of the absolute magnitude, as well as the three vector components. In a different representation, the reconstructed spatio-mean velocity $\vec{v}(t)$ of each heart chamber was plotted in 3D space over time. Additionally, velocity histograms for each cardiac bin and for each heart chamber, i.e. RA, RV, LA and LV, were computed for the representative cardiac cycle.

III. Results

A. Experimental Part

Fig. 3 shows the ParaVision GUI, in which the non-relocatable MPI-FoV is represented by overlay boxes onto the low-resolution MRI data. The low-resolution MRI data was used for manual subject positioning to locate the heart as target region into the non-relocatable MPI-FoV. High-resolution MRI MSME morphological datasets are shown in Fig. 4 for the pre- and post-injection acquisition, representing the final subject position.

B. Data Post-Processing and Data Analysis

In Fig. 5, the MRI-based movement assessment depicted as error map $\epsilon(p)$ comparing the pre- and post-injection coronal MSME dataset is shown. It proves the subject's position retention during the entire experimental procedure. For validation, an excellent agreement is achieved after shifting the post-injection dataset by one pixel (i.e. 0.39 mm) in Le-Rt (read) direction. The main deviation between pre- and post-injection MRI data are concentrated in the liver tissue by means of signal voids of -35% in the post-injection MRI data. Within the heart and the blood-pool, the relative error between pre- and post-injection MRI data shows a signal deviation of solely -3%.

The fused and co-registered hybrid dataset is shown in Fig. 6 at 5 different time points in tri-planar orthogonal views, as well as in a volume rendered representation. The respective time points are indicated in the TIC of the global MPI-derived VOI and depict the background signal prior to the bolus, the tracer inflow of the first passage, the bolus maximum, the second maximum caused by the return flow from the lungs as well as the bolus fade-out. Videos of the orthogonal and volume rendered visualization shown in Fig. 6 are provided as supplementary material ***S1*** and ***S2*** to this manuscript.

Fig. 7a shows the MR-derived VOIs while Fig. 7d depicts the VOIs cropped along the MPI DF-FoV used hereafter for all further analysis. Table I summarizes the VOI volumes and ratios of the cropped VOI versions. On basis of the different VOIs, the MPI signal TICs of the respective spatial positions and their Fourier-transform are highlighted in Fig. 8a (top) and 8b, respectively.

For the MPI-based optical flow based velocity estimation, the effect of the Tikhonov optical flow regularization is shown in Fig. 9, which served as input for the pre-adjustment step. The manually selected λ is highlighted as vertical line in Fig. 9. Results of the real-time MPI-based optclfw velocity estimation are shown in form of TVCs (c.f. Fig. 8 bottom) and in a 3D streamline representation (c.f. Fig. 10) superimposed with the three orthogonal, high-spatial resolution MRI pre-injection datasets. An animated 3D + t representation of the real-time flow estimation is appended as supplementary material ***S3*** to this manuscript.

The result of the virtual representative cardiac cycle is presented as TVCs (c.f. Fig. 11). In this figure, the vector decomposition ($\vec{v}_x(t)$, $\vec{v}_y(t)$, $\vec{v}_z(t)$) of the reconstructed velocities for each cardiac bin is shown. For visual guidance, a spline interpolation was used to connect the data points. Vector representations of the virtual cardiac cycle are shown in Fig. 12 for the heart chambers RA, RV, LA and LV, respectively. Velocity histograms are shown in Fig. 13 for all cardiac bins and heart chambers. An animated 3D + t representation of the representative cardiac cycle is appended as supplementary material ***S4*** to this manuscript.

IV. Discussion

Data acquisition of all hybrid MPI-MRI data used in this contribution was realized by using one highly integrated MPI-MRI hybrid system (c.f. Fig. 1) in a closed experimental, sequential *in situ* setup as depicted in Fig. 2. A seamless hybrid imaging study was facilitated by using a ParaVision 6.1 imaging platform. After the first step of MR-guided animal positioning with respect to the non-relocatable MPI-FoV (c.f. Fig. 3), the final subject position was preserved during the entire *in situ* dual-modal cardiovascular assessment. As the intrinsic FoV of MPI is rather small (here DF-FoV $22 \times 22 \times 11$ mm^3), precise and reliable morphological planning of the target region is essential. This was enabled by the preferred implementation of an integrated hybrid imaging system with imaging-centers matching each other. Using the maximal polarization field of the used hybrid imaging system of approx. 0.5 T, high-spatial resolution MSME MRI datasets were acquired in the final subject position (c.f. Fig. 4a-4c), serving as high quality morphological reference datasets. After switching into the MPI-mode, the injected SPION bolus passage was successfully recorded and reconstructed (c.f. 6a) prior to switching the system back into the MRI mode. The modality transition was performed in either direction within approx. 2 min, while an additional waiting time of approx. 10 min is beneficial to reach maximal MRI field stability in the range of 45 Hz/min (i.e. 2 ppm/min) preventing thermal induced field drifts. Due to the fully dual-modal compatible system design which prevents any system hardware modifications, the subject's position remained unchanged during the entire *in situ* dual-modal experiment. Neither the post-injection MRI data (c.f. Fig. 4d) itself, nor the error maps for the MRI-based movement assessment comparing the pre- and post-injection coronal MRI data, shown in Fig. 5, highlight any adverse effects of the scan mode switching (MRI to MPI, and MPI to MRI). Furthermore, this MR-based comparison proves the subject position reliability during the entire *in situ* dual-modal cardiovascular assessment. This assessment justified the choice of compensating only the constant modality specific coordinate offsets [23]. The remaining residual one voxel off-

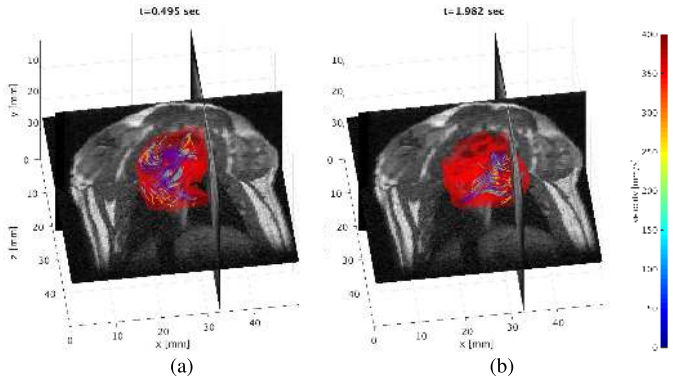

Fig. 10. 3D view of the real-time flow estimation represented as color-coded streamlines superimposed with the morphological information acquired by a high-resolution MSME MRI protocol. The time dependent red translucent isosurface represents the modulus threshold derived in the Flow Analysis Toolbox which illustrates the blood volume. This surface served as a boundary condition for the flow analysis computation. The 3D + t velocity vector field is shown in streamlines, whereas the color encodes $|\vec{v}(t)|$ in mm/s. (a)-(b) represent two different time points of the real-time 3D + t flow analysis. An animated 3D + t representation of the real-time flow estimation is appended as supplementary material ***S3*** to this manuscript.

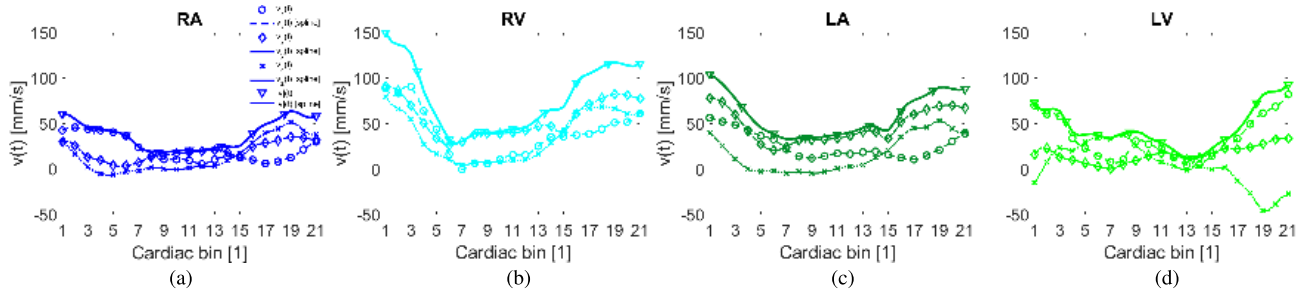

Fig. 11. Vector decomposition of the 3D + t velocity vector field of one representative cardiac cycle. (a)-(d) depict the Time-Velocity-Curve (TVC) within the MR-derived VOIs of the four heart chambers from left to right RA, RV, LA and LV, respectively. The reconstructed values for all 21 cardiac bins are shown with markers, while spline interpolations thereof are represented by lines. The reconstructed temporal resolution is 10 ms per cardiac bin. The scaling of the individual plots are kept identical.

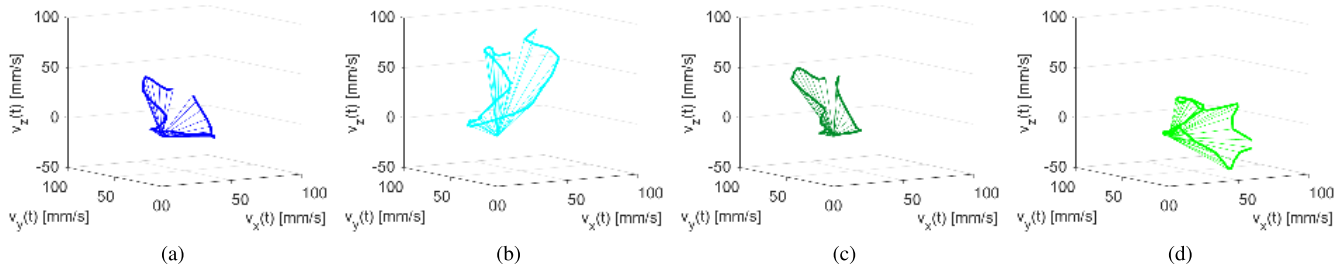

Fig. 12. Spatio-mean velocity vector visualization of one representative cardiac cycle reconstructed into 21 cardiac bins. (a)-(d) depict the TVC of the four heart chambers from left to right RA, RV, LA and LV, respectively. The scaling of the individual plots is kept identical.

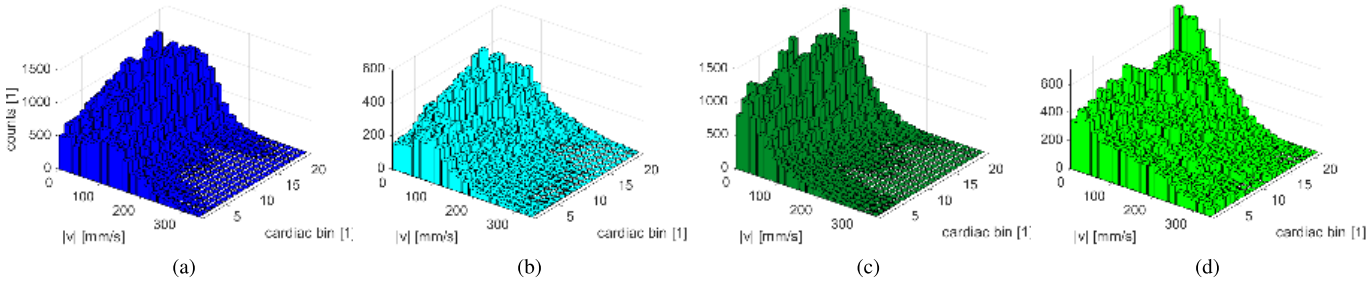

Fig. 13. Velocity histograms of the 3D + t velocity vector field of one representative cardiac cycle shown for the four MR-derived VOIs from left to right RA, RV, LA and LV, respectively.

set visible in the read direction (Le-Rt) between both datasets most likely results from a non-compensated B_0 field drift corresponding to 9 ppm which translates into $\Delta B_0 = 4.5\,\mu$T. In the post-injection MRI dataset, the expected effect of SPION accumulation within the liver can be seen by hypo-intense signal areas. The liver tissue presents a significantly decreased signal intensity of -35%, compared to the pre-injection MSME data.

MPI 3D + t image reconstruction of the bolus passage with a temporal resolution of 21.54 ms/volume was achieved with high SNR using the background corrected MPI raw data. Using a pre-determined global translation [23] (-2.5 mm, -1 mm, -1.5 mm for X-, Y- and Z-direction, respectively) to the reconstructed MPI data allowed high precise dual-modal data fusion as presented in Fig. 6 (b)-(k). In addition to the Time-Intensity-Curve in Fig. 6 (a) of the entire MPI-signal VOI, the fused orthogonal views (c.f. Fig. 6 (b)-(f)) and volume rendered representation (c.f. Fig. 6 (g)-(k)) are presented for selected time points depicting the baseline (b), the bolus inflow into the right heart chambers (c)-(d) and left heart chambers (e), as well as the first-pass bolus fade out (f). To fully represent the high temporal resolution 3D + t dataset, an animated 3D + t representation of the fused dual-modal dataset is appended to this manuscript. The supplementary material ***S1*** and ***S2*** depict clearly the bolus envelope from the first SPION inflow to the bolus fade-out with distinct pseudo-periodic signal-variations, caused by the heart contractions.

In the TIC of the MPI-signal VOI shown in Fig. 8, no significant modulation of the tracer concentration is visible. This is reasonable, as this VOI depicts the volume integral and thus represents the envelope of the SPION bolus. Furthermore, deriving precise morphological VOIs from MPI data is non-trivial. This can be seen by comparing the MPI-derived (0.73 ccm) signal volume and the total MR-derived heart volume (1.7 ccm), cropped to the DF-FoV (c.f. Table I). The high-resolution pre-injection MSME coronal dataset, on the other hand, allowed precise segmentation of static morphological

VOIs (c.f. Fig. 7) representing the four heart chambers RA, RV, LA and LV, as well as the lungs. To allow for trustworthy MPI analysis, only reconstructed image intensities within the confidence interval defined by the DF-FoV were used. This can be seen in Fig. 7d, where the MR-derived VOIs are cropped along the DF-FoV. In Table I, the segmented volumes, as well as the volumes cropped to the DF-FoV (comparing Fig. 7a and 7d) are presented next to the respective ratio of the volumes covered by the DF-FoV. Table I shows that approx. 83% of the total MR-derived heart volume is covered by the MPI DF-FoV. Only the volumes cropped to the DF-FoV were used for the presented cardiovascular assessment. Using the here-presented hybrid system, a full coverage of the heart volume by the MPI DF-FoV could be realized only by either a reduced MPI *Selection Field* gradient strength or an increased *Drive Field* amplitude. A reduction of the gradient strength was not chosen in order to maximize the spatial resolution capability [7] of the system, while the maximal *Drive Field* amplitude allowed by the system was already reached.

The time-intensity curves in Fig. 8 are derived from the MR-guided segmentation of the 3D + t MPI dataset. Sequentially, the maximum signal intensity resulting from the bolus passage occurs in the right atrium, right ventricle, the lungs, left atrium, and left ventricle, in accordance with physiological function. This confirms that the chosen strategy of data fusion and analysis of the dual-modal experiment enables a reliable interpretation of the time-dependent MPI signal intensity that provides additional information not readily obtained from the standalone modalities. The total signal intensity from the entire DF-FoV only exhibits a minor modulation which is consistent with the heartbeat, caused by a partial volume effect of the entire heart moving in the limited DF-FoV. Conversely, a strong signal modulation is evident in the TICs derived from the individual segmented heart chambers, caused by the specific stages of blood transport during the cardiac cycle. Specifically, a near 180° phase shift is observed between the TICs derived from the atria and the adjacent ventricle as a consequence of blood inflow during ventricular late diastole, while both atria, as well as both ventricles depict a common phase due to the coordinated and synchronous contraction. By evaluating the RV-peak and the LA-peak in Fig. 8a, there is a time shift of approx. 1 s resulting from the passage time through the pulmonary circuit. This value is in accordance with the TIC results in [32]. In Fig. 8a, furthermore, the TIC belonging to the lung VOI presents its signal peak between the signal peaks of the right heart and the signal peaks of the left heart. Voxels neither assigned to the heart chambers, nor to the lungs do not exhibit significant signal intensities at any time, confirming the accurate co-registration of the MPI data to the MRI data. One can further deduce that the breathing cycle and the resulting respiratory induced motion is small and thus justifies in first instance the usage of static VOIs. However, by analyzing the Fourier-transformed TICs presented in Fig. 8b, despite the cardiac frequency of 4.9 Hz, as well as two harmonics thereof, i.e. 9.8 Hz and 14.7 Hz, one can find a peak at 0.9 Hz, depicting the respiratory frequency. This finding is in close accordance with the respiration rates measured within the range of 40−60 bpm acquired with a respiratory sensor for vital parameter supervision during the dual-modal cardiovascular assessment.

A previous simulation study [30] has shown a significant impact of the Tikhonov regularization onto the reconstructed velocity estimates. It was found that in the used optical flow analysis a high λ underestimates the velocities while a low λ produces local overestimates. The same effect holds true for the *in vivo* data presented in this contribution as shown in Fig. 9. As a compromise, $\lambda = 10^{-11}$ was chosen for which the spatio-temporal mean velocity is preserved while local overestimates are significantly damped. The MPI-based 3D + t velocity vector estimation, presented in Fig. 8a (bottom), were reconstructed for a sub-sequence of approx. 3 s of MPI data. This time range comprises the bolus in- and outflow into the right, as well as the left heart chambers. This sub-sequence is highlighted by the gray background in Fig. 8a. Thus, the flow analysis is based on input data acquired without respiratory and cardiac gating and under free-breathing condition. The real-time 3D + t velocity vector estimate shown in Fig. 8a as time-velocity-curves (TVCs) was reconstructed with a time resolution of 10 ms using the deduced Tikhonov regularizer $\lambda = 10^{-11}$. A phase shift of approx. 90° between TICs and their respective TVCs can be seen, explained by the fact that a tracer concentration and tracer volume change occurs in answer to blood flow. In Fig. 10, the real-time flow estimate is represented in velocity magnitude color-coded streamlines superimposed with the three orthogonal high-resolution pre-injection MRI datasets for morphological guidance. Two different time points have been chosen representing the inflow into the right and the left heart, respectively. The supplementary material ***S3*** presents complex real-time flow pattern with coherent streamlines and velocity magnitudes well above 300 mm/s for the entire reconstructed sequence of approx. 3 seconds.

Boiling down the complexity of the real-time 3D + t dataset and to compress the flow information of the bolus, one virtual representative cardiac cycle containing 21 bins was computed. This virtual cardiac cycle is shown in Fig. 11, 12 and 13 in different representations. Here, spatio-mean velocity values within the different anatomical MR-derived VOIs (RA, RV, LA, LV) are presented as TVCs (c.f. Fig. 11 and 12) and time resolved velocity histograms (c.f. Fig. 13). By applying vector decomposition, the velocity components for each spatial dimension are presented in Fig. 11 individually for each reconstructed cardiac bin complemented for visual guidance with a spline interpolation thereof. The spatio-mean TVCs of all VOIs highlight the maximum velocity at cardiac bin number 1, while the first and the last cardiac bin are close by each other which is a prerequisite for a (pseudo) periodic velocity evolution. This is in accordance with the data sorting based on the TIC of the RA, where the max. values were used for the starting point of individual cardiac cycles. This can also be seen in Fig. 12 in which the spatio-mean velocity vector is shown in 3D space over time. By comparing the TVCs of the right atrium (c.f. Fig. 11a/12a) and the left atrium (c.f. Fig. 11c/12c), one can see a high similarity in terms of magnitude and direction of the estimated blood flow. On the other hand, the atria and the ventricle depict

significantly different velocity patterns while the two ventricles (c.f. Fig. 11b/12b and Fig. 11d/12d) also differ significantly. The left ventricular blood flow pattern shown in Fig. 11d/12d is known to form a complex spatial and temporal flow pattern including vortices [33], as well as complex contraction patterns inducing rotational movements [34]. In late diastole, ventricles are filled by an atrial kick, therefore the inflow tracts show the highest blood flow velocities. With approx. 150 mm/s the right ventricle presents the highest spatio-mean velocity magnitude (c.f. Fig. 11b). The velocity magnitudes in the TVC representation with maxima in the range of 60−150 mm/s (c.f. Fig. 11) are approx. a factor of 3 lower compared to the 3D + t representation in Fig. 10. This can be explained as partial volume effect caused by volume averaging of inhomogeneous velocity distributions over space, i.e. the VOIs. The velocity value distribution within the different VOIs are presented in Fig. 13 as velocity histograms. Inhomogeneous velocity values within large evaluation volumes containing solid boundaries are expected in laminar, as well as turbulent flows. Compared to all other heart chambers, the velocity histograms of both ventricles RV and LV, shown in Fig. 13b and 13d, exhibit the broadest velocity distribution and the highest velocity magnitudes well above 300 mm/s. Likewise, the maximum velocity magnitudes of approx. 1000 mm/s in Fig. 9 are in accordance with the findings in [35]. Evaluating the spatially-resolved velocity vector field of the virtual representative cardiac cycle, presented in the animated velocity magnitude color-coded streamlines superimposed with the three orthogonal high-resolution pre-injection MRI datasets for morphological guidance (supplementary material ***S4***), support the physiological findings in [35]. Inhere, coherent streamlines form local jets with reconstructed velocities well above 300 mm/s. Furthermore, pseudo-periodic contractions and pseudo-periodic velocity variations can be observed throughout the entire vector field.

V. Conclusion

With this work, the first *in vivo* MPI-based 3D + t flow analysis superimposed with morphological reference MRI data was shown. Furthermore, this dual-modal cardiovascular assessment on a rat is the first reported *in vivo* experiment performed *in situ* on a highly integrated MPI-MRI hybrid system without the need for animal repositioning in a single seamless study. Morphological MR-guidance for MPI-FoV planning allowed a best fit organ targeting and is a key factor for high throughput *in vivo* bolus imaging. Morphological data acquired in the MRI-mode at approx. 0.5 T are sufficient for manual segmentation of the four heart chambers, as well as the lungs. Reliable and straight forward multi-modal data fusion is an additional advantage of integrated hybrid systems which allows for the first precise MR-based functional MPI analysis with highly reduced co-registration uncertainties. Additionally, pre- and post-injection MRI datasets directly allow verification of the subject position reliability during the entire study. MR-based VOI generation permits precise segmentation of the low-spatial resolution MPI data. This segmentation is the basis of a full spatio-temporal analysis providing detailed insight into quantitative cardiac parameters. In this work, local evolutions of the tracer distribution has been presented as TICs, whereas velocity estimates have been presented in 3D + t in real-time and as a retrospectively gated virtual cardiac cycle.

New techniques which allow for the assessment hemodynamic velocities in a single shot examination are of great potential. Besides primary prevention of cardiac diseases, this technique could be beneficial for continuous or repetitive monitoring of intensive care unit patients after coronary artery bypass or in critical illnesses like cardiac shock. In this study, the dual-modal cardiac assessment was demonstrated on the hemodynamics of a beating rat's heart by analyzing MPI data acquired in an ungated sequence under free-breathing conditions. Deriving additional metrics, such as cardiac output fractions or pressure estimations from the velocity estimation are in reach and in scope of further investigations.

Translating the presented MPI-MRI hybrid approach to human applications [36] would necessitate large FoV imaging sequences using *Focus Field* coil sets allowing for patched data acquisition schemes [37]. Such homogenous shift field coils were not implemented in the pre-clinical MPI-MRI hybrid system demonstrator used in this contribution to not increase the system's complexity. The B_0 magnetic field strength of 0.5 T realized as resistive magnet in the described demonstrator [20] is sufficient for a pre-clinical feasibility study and manual segmentation, however bears limitations in a clinical setting. Superconductive hybrid MPI-MRI magnet designs, such as [17] are however in reach, featuring B_0 magnetic field strength commonly used in clinical systems and which are scalable to human sized hybrid systems. Furthermore, in-line MPI-MRI system designs omit modality switching times and allow independent modality specific optimization by e.g. bringing the receive detectors as close as possible to the object. In a clinical setup, the proposed dual-modal *in situ* cardiovascular assessments can therefore be translated into an examination with low patient preparation effort and high patient comfort. The option to generate a virtual cardiac cycle could facilitate the diagnosis of cardiac malfunction, such as valvular stenosis or insufficiency, especially mitral or aortic valve diseases. These diagnoses are currently evaluated primarily by ultrasound, while the procedure is highly dependent on the occupational qualification and physiological acoustic windows.

In this study, all time resolved information was derived from MPI data acquired within approx. 3 s containing the first passage of a 21 μl SPION bolus. This SPION bolus translates to 40 μmol(Fe)/kg$_{BW}$ which is 4-fold the approved clinical diagnostic dosage. Our work highlights the benefits of integrated MPI-MRI hybrid systems which permit acquisition of both morphological and functional data in a seamless dual-modal study and with high confidence in data co-registration. We have shown the versatility of an integrated MPI-MRI hybrid system and the ability of anatomical targeting bolus imaging with the hot-spot imaging technique Magnetic Particle Imaging. With this contribution, we have presented the first *in-vivo* results of a new methodology, allowing for fast, non-

invasive, quantitative and *in situ* hybrid cardiovascular assessment, showing its potential for future clinical applications.

ACKNOWLEDGMENT

All animal experiments were performed with the legal approval of the responsible Animal Ethics Committee (Regional Council of Karlsruhe), Germany. The authors thankfully acknowledge Doyin Adewunmi, Dr. Dominik von Elverfeldt, and Dr. Sarah-Rebecca Herrmann for proofreading of this manuscript.

REFERENCES

[1] L. Martí-Bonmatí, R. Sopena, P. Bartumeus, and P. Sopena, "Multimodality imaging techniques," *Contrast Media Mol. Imag.*, vol. 5, no. 4, pp. 180–189, Jul. 2010.

[2] T. Beyer *et al.*, "A combined PET/CT scanner for clinical oncology," *J. Nucl. Med.*, vol. 41, no. 8, pp. 1369–1379, 2000.

[3] G. Delso *et al.*, "Performance measurements of the siemens mMR integrated whole-body PET/MR scanner," *J. Nucl. Med.*, vol. 52, no. 12, pp. 1914–1922, 2011.

[4] B. Weissler *et al.*, "A digital preclinical PET/MRI insert and initial results," *IEEE Trans. Med. Imag.*, vol. 34, no. 11, pp. 2258–2270, Nov. 2015.

[5] J. Zhang, J. Chen, B. Cheong, A. Pednekar, and R. Muthupillai, "High frame rate cardiac cine MRI for the evaluation of diastolic function and its direct correlation with echocardiography," *J. Magn. Reson. Imag.*, vol. 50, no. 5, pp. 1571–1582, Nov. 2019.

[6] B. Gleich and J. Weizenecker, "Tomographic imaging using the nonlinear response of magnetic particles," *Nature*, vol. 435, no. 7046, pp. 1214–1217, Jun. 2005.

[7] J. Rahmer, J. Weizenecker, B. Gleich, and J. Borgert, "Signal encoding in magnetic particle imaging: Properties of the system function," *BMC Med. Imag.*, vol. 9, no. 1, p. 4, Dec. 2009.

[8] X. Y. Zhou *et al.*, "First *in vivo* magnetic particle imaging of lung perfusion in rats," *Phys. Med. Biol.*, vol. 62, no. 9, p. 3510, 2017.

[9] B. Zheng *et al.*, "Quantitative magnetic particle imaging monitors the transplantation, biodistribution, and clearance of stem cells *in vivo*," *Theranostics*, vol. 6, no. 3, p. 291, 2016.

[10] D. Pantke, N. Holle, A. Mogarkar, M. Straub, and V. Schulz, "Multifrequency magnetic particle imaging enabled by a combined passive and active drive field feed-through compensation approach," *Med. Phys.*, vol. 46, no. 9, pp. 4077–4086, Sep. 2019.

[11] J. Weizenecker, B. Gleich, J. Rahmer, H. Dahnke, and J. Borgert, "Three-dimensional real-time *in vivo* magnetic particle imaging," *Phys. Med. Biol.*, vol. 54, no. 5, p. 1, 2009.

[12] P. Ludewig *et al.*, "Magnetic particle imaging for real-time perfusion imaging in acute stroke," *ACS Nano*, vol. 11, no. 10, pp. 10480–10488, Oct. 2017.

[13] M. Graeser *et al.*, "Towards picogram detection of superparamagnetic iron-oxide particles using a gradiometric receive coil," *Sci. Rep.*, vol. 7, no. 1, pp. 1–13, Dec. 2017.

[14] E. Y. Yu *et al.*, "Magnetic particle imaging for highly sensitive, quantitative, and safe *in vivo* gut bleed detection in a murine model," *ACS Nano*, vol. 11, no. 12, pp. 12067–12076, 2017.

[15] M. G. Kaul *et al.*, "Magnetic particle imaging for *in vivo* blood flow velocity measurements in mice," *Phys. Med. Biol.*, vol. 63, no. 6, Mar. 2018, Art. no. 064001.

[16] J. Franke *et al.*, "First hybrid MPI-MRI imaging system as integrated design for mice and rats: Description of the instrumentation setup," in *Proc. Int. Workshop Magn. Part. Imag. (IWMPI)*, Mar. 2013, p. 1.

[17] J. Franke, U. Heinen, V. Niemann, M. Heidenreich, and T. Buzug, "Alternative hybrid MPI-MRI imaging system design: Superconductive field generator topology," in *Proc. Int. Workshop Magn. Part. Imag. (IWMPI)*, Mar. 2013, p. 1.

[18] P. Vogel *et al.*, "MRI meets MPI: A bimodal MPI-MRI tomograph," *IEEE Trans. Med. Imag.*, vol. 33, no. 10, pp. 1954–1959, Oct. 2014.

[19] P. Klauer, P. Vogel, M. A. Ruckert, W. H. Kullmann, P. M. Jakob, and V. C. Behr, "Bimodal TWMPI-MRI hybrid scanner—Coil setup and electronics," *IEEE Trans. Magn.*, vol. 51, no. 2, pp. 1–4, Feb. 2015.

[20] J. Franke *et al.*, "System characterization of a highly integrated preclinical hybrid MPI-MRI scanner," *IEEE Trans. Med. Imag.*, vol. 35, no. 9, pp. 1993–2004, Sep. 2016.

[21] P. Vogel *et al.*, "Magnetic particle imaging meets computed tomography: First simultaneous imaging," *Sci. Rep.*, vol. 9, no. 1, pp. 1–9, 2019.

[22] T. C. Kranemann, T. Ersepke, and G. Schmitz, "Towards the integration of an MPI compatible ultrasound transducer," *Int. J. Magn. Part. Imag.*, vol. 3, no. 1, pp. 1–9, 2017.

[23] J. Franke *et al.*, "Evaluation of the spatial confidence and dual modal FOV-center conformity of a highly integrated MPI-MRI hybrid system," in *Proc. Int. Workshop Magn. Part. Imag. (IWMPI)*, 2016, p. 34.

[24] M. Grüttner *et al.*, "On the formulation of the image reconstruction problem in magnetic particle imaging," *Biomedizinische Technik/Biomed. Eng.*, vol. 58, no. 6, pp. 583–591, Jan. 2013.

[25] S. Kaczmarz, "Angenaeherte aufloesung von systemen linearer Gleichungen," *Bull. Int. de l'Académie Polonaise des Sci. et des Lettres*, vol. 35, no. 35, pp. 355–357, 1937.

[26] A. Weber, J. Weizenecker, U. Heinen, M. Heidenreich, and T. M. Buzug, "Reconstruction enhancement by denoising the magnetic particle imaging system matrix using frequency domain filter," *IEEE Trans. Magn.*, vol. 51, no. 2, pp. 1–5, Feb. 2015.

[27] A. Weber, F. Werner, J. Weizenecker, T. M. Buzug, and T. Knopp, "Artifact free reconstruction with the system matrix approach by overscanning the field-free-point trajectory in magnetic particle imaging," *Phys. Med. Biol.*, vol. 61, no. 2, p. 475, 2015.

[28] R. Lacroix, "3D optical flow analysis of a pulsed contrast agent in the bloodstream. Application to virtual angiography and magnetic particle imaging," Doctoral dissertation, Télécom Bretagne, Université de Bretagne Occidentale, Brest, France, 2015.

[29] J. Franke, R. Lacroix, H. Lehr, M. Heidenreich, U. Heinen, and V. Schulz, "MPI flow analysis toolbox exploiting pulsed tracer information–an aneurysm phantom proof," *Int. J. Magn. Part. Imag.*, vol. 3, no. 1, pp. 1–5, 2017.

[30] J. Franke, R. Lacroix, H. Lehr, and V. Schulz, "MPI based 4d flow estimation–a simulation study," in *Proc. Int. Workshop Magn. Part. Imag. (IWMPI)*, 2018, pp. 91–92.

[31] B. D. Lucas and T. Kanade, "An iterative image registration technique with an application to stereo vision," in *Proc. Int. Joint Conf. Artif. Intell.*, Vancouver, BC, Canada, Aug. 1981, pp. 674–679.

[32] N. N. Mistry, J. Pollaro, J. Song, M. De Lin, and G. A. Johnson, "Pulmonary perfusion imaging in the rodent lung using dynamic contrast-enhanced MRI," *Magn. Reson. Med.*, vol. 59, no. 2, pp. 289–297, 2008.

[33] T. Yano, M. Funayama, S. Sudo, and Y. Mitamura, "Analysis of flow within a left ventricle model fully assisted with continuous flow through the aortic valve," *Artif. Organs*, vol. 36, no. 8, pp. 714–723, Aug. 2012.

[34] H. Zhang *et al.*, "The left ventricular intracavitary vortex during the isovolumic contraction period as detected by vector flow mapping," *Echocardiography*, vol. 29, no. 5, pp. 579–587, May 2012.

[35] L. E. Watson, M. Sheth, R. F. Denyer, and D. E. Dostal, "Baseline echocardiographic values for adult male rats," *J. Amer. Soc. Echocardiography*, vol. 17, no. 2, pp. 161–167, Feb. 2004.

[36] J. Borgert *et al.*, "Perspectives on clinical magnetic particle imaging," *Biomedizinische Technik/Biomed. Eng.*, vol. 58, no. 58, pp. 551–556, 2013.

[37] J. Rahmer *et al.*, "Results on rapid 3D magnetic particle imaging with a large field of view," in *Proc. Int. Soc. Magn. Reson. Med.*, Montréal, QC, Canada, vol. 19, 2011, p. 629.